Flight–crash events in turbulence

Haitao Xu[a,b], Alain Pumir[a,b,c], Gregory Falkovich[a,d,e], Eberhard Bodenschatz[a,b,f,g,1], Michael Shats[h], Hua Xia[h], Nicolas Francois[h], and Guido Boffetta[a,i]

[a]International Collaboration for Turbulence Research, D-37077 Göttingen, Germany; [b]Max Planck Institute for Dynamics and Self-Organization, D-37077 Göttingen, Germany; [c]Laboratoire de Physique, Ecole Normale Supérieure de Lyon, Université de Lyon 1 and Centre National de la Recherche Scientifique, F-69007 Lyon, France; [d]Physics of Complex Systems, The Weizmann Institute of Science, Rehovot 76100, Israel; [e]Institute for Information Transmission Problems, Moscow 127994, Russia; [f]Institute for Nonlinear Dynamics, University of Göttingen, D-37077 Göttingen, Germany; [g]Laboratory of Atomic and Solid State Physics and Sibley School of Mechanical and Aerospace Engineering, Cornell University, Ithaca, NY 14853; [h]Research School of Physics and Engineering, The Australian National University, Canberra, ACT 0200, Australia; and [i]Department of Physics and Istituto Nazionale di Fisica Nucleare, University of Torino, I-10125 Turin, Italy

Edited by Harry L. Swinney, University of Texas at Austin, Austin, TX, and approved March 24, 2014 (received for review November 20, 2013)

The statistical properties of turbulence differ in an essential way from those of systems in or near thermal equilibrium because of the flux of energy between vastly different scales at which energy is supplied and at which it is dissipated. We elucidate this difference by studying experimentally and numerically the fluctuations of the energy of a small fluid particle moving in a turbulent fluid. We demonstrate how the fundamental property of detailed balance is broken, so that the probabilities of forward and backward transitions are not equal for turbulence. In physical terms, we found that in a large set of flow configurations, fluid elements decelerate faster than accelerate, a feature known all too well from driving in dense traffic. The statistical signature of rare "flight–crash" events, associated with fast particle deceleration, provides a way to quantify irreversibility in a turbulent flow. Namely, we find that the third moment of the power fluctuations along a trajectory, nondimensionalized by the energy flux, displays a remarkable power law as a function of the Reynolds number, both in two and in three spatial dimensions. This establishes a relation between the irreversibility of the system and the range of active scales. We speculate that the breakdown of the detailed balance characterized here is a general feature of other systems very far from equilibrium, displaying a wide range of spatial scales.

nonequilibrium systems | turbulent mixing | direct and inverse turbulent energy cascades | nonequilibrium statistical mechanics | Lagrangian description

In systems at thermal equilibrium, the probabilities of forward and backward transitions between any two states are equal, a property known as "detailed balance." This fundamental property expresses time reversibility of equilibrium statistics (1). In the important class of nonequilibrium problems, where the dynamics of the system is coupled with a heat bath, the notion of detailed balance can be extended and fluctuation theorems successfully describe the behavior (2, 3). This class contains many experimental situations (4) where quantitative information on irreversibility was obtained (3). When a system driven by thermal noise is characterized by a probability current, the fluctuation–dissipation theorem and detailed balance was found to apply in a comoving reference frame (5).

In comparison, very little is known concerning the statistical properties of a small part embedded in a fluctuating, turbulent background. The fundamental notion of detailed balance is not expected to apply in such systems. Here we ask, what does the time irreversibility inherent to the large system imply for the statistical properties of small parts in the system and how do we measure the degree of irreversibility (6, 7) (or equivalently, how far is the system away from equilibrium) by monitoring a small part in the system? We focus here on fluid turbulence, a paradigm for ultimate far-from-equilibrium states, where irreversibility of fluctuations is a fundamental property (8, 9). We show that the simplest and most fundamental scalar quantity, namely, the kinetic energy of a fluid particle, enables a clear identification and quantification of the irreversibility of the turbulent flow.

The characteristic properties of turbulence rest on the vastly different scales: from the scale l_F, where the flow is forced and inertia dominates, to the scale l_D, where dissipation takes over. For a balance between forcing and dissipation in a statistically steady flow, energy is transferred through scales at an average rate ε, a phenomenon called "energy cascade." In 3D flows, where $l_F \gg l_D$ (9, 10), energy cascades from large to small scales. In contrast, energy transfers from small to large scales in 2D flows, where $l_F \ll l_D$ (11, 12). The energy flux is ultimately the source of statistical irreversibility. It is important to understand that the fluctuations in turbulence are fundamentally different from those about thermal equilibrium (8). The energy flux through scales, ε, however, cannot in itself be a measure of irreversibility in the system because ε is a dimensional quantity, so it can be made arbitrarily large by changing the units even if the system is very close to equilibrium. Moreover, it can be expressed as a moment of velocity differences at a single time (10, 13) without any reference to the evolution of the flow.

As we demonstrate below, the irreversibility induced by the energy flux through spatial scales can be revealed and quantified by following the change of the kinetic energy of small fluid elements (particles). The kinetic energy per unit mass of the fluid is simply $E(t) = (1/2)V^2(t)$, where $\mathbf{V}(t)$ is the velocity of a given fluid element. It should be stressed that detecting irreversibility from the motion of a single particle requires going beyond velocity structure functions, defined as the moments of velocity differences along trajectories, $\mathbf{V}(t) - \mathbf{V}(0)$, whose statistical properties are invariant under the $t \to -t$ transformation (14).

Significance

Irreversibility is a fundamental aspect of the evolution of natural systems, and quantifying its manifestations is a challenge in any attempt to describe nonequilibrium systems. In the case of fluid turbulence, an emblematic example of a system very far from equilibrium, we show that the motion of a single fluid particle provides a clear manifestation of time irreversibility. Namely, we observe that fluid particles tend to lose kinetic energy faster than they gain it. This is best seen by the presence of rare "flight–crash" events, where fast moving particles suddenly decelerate into a region where fluid motion is slow. Remarkably, the statistical signature of these events establishes a quantitative relation between the degree of irreversibility and turbulence intensity.

Author contributions: H. Xu, A.P., G.F., and E.B. designed research; H. Xu, A.P., G.F., E.B., M.S., H. Xia, N.F., and G.B. performed research; H. Xu, A.P., G.F., E.B., M.S., H. Xia, N.F., and G.B. analyzed data; and H. Xu, A.P., G.F., and E.B. wrote the paper.

The authors declare no conflict of interest.

This article is a PNAS Direct Submission.

[1]To whom correspondence should be addressed. E-mail: eberhard.bodenschatz@ds.mpg.de.

This article contains supporting information online at www.pnas.org/lookup/suppl/doi:10.1073/pnas.1321682111/-/DCSupplemental.

The recent advances in our ability to reliably measure the trajectories of small tracer particles in well-controlled laboratory flows (15–18), as well as to simulate accurately the motion of particle tracers using the Navier–Stokes equation (16) allow us to investigate these fundamental issues. In this work, we restrict ourselves to statistically stationary and homogeneous flows. The results shown here were obtained from a variety of flow configurations in 2D and 3D, including both laboratory experiments and direct numerical simulations of the Navier–Stokes equations. The datasets contain a large number of trajectories, with at least 10^8 data points in total, both in 2D and 3D (see *Materials and Methods* and *SI Text* for details).

Results

"Flight–Crash" Events. The phenomenon discussed here is illustrated in Fig. 1 *A* and *B*, which show the evolution of $E(t)$ along the trajectory of a fluid particle in a 3D laboratory water flow (17, 18). It illustrates that to build up large kinetic energy requires a longer time than to dissipate the same amount. This points to the occurrence of flight–crash like events, whereby a particle flies with a large velocity, before suddenly losing energy. This feature, which we also observed in numerical simulation of turbulent flows, is reminiscent of what occurs in very different systems, such as cars in traffic (19) or even fluctuations of stock values (20).

Statistics of Energy Difference. The statistics of the energy increments, $W(\tau)=E(t+\tau)-E(t)$, are sensitive to the flight-crash events. We stress that the moments of $W(\tau)$ cannot be expressed in terms of Lagrangian velocity structure functions, and notice that the kinetic energy $E(t)$ is not Galilean invariant, which we further discuss in *SI Text*. The asymmetry revealed by Fig. 1 implies that the distribution of $W(\tau)$ is skewed: Odd moments are expected to be negative for $\tau>0$. For stationary, homogeneous flows, the first moment vanishes, $\langle W(\tau)\rangle=0$. The first nonvanishing odd moment, $-\langle W^3(\tau)\rangle$, measured from both experiments and numerical simulations (18) of 3D turbulence is shown in Fig. 2*A*. In all these flows, $-\langle W^3(\tau)\rangle$ grows as τ^3 at short times, then slower at intermediate times, and remains positive over the entire range of turbulence dynamical time scales. [Negative skewness of $u_x^2(t)-u_x^2(0)$, where u_x is one velocity component of a tracer particle in a 3D turbulence flow, was also reported by Mordant (21).] Fig. 2*B* shows that the third moment of $W(\tau)$ in 2D is similar to those in 3D (Fig. 2*A*), i.e., it is independent of the difference in the direction of the energy flux in 2D and 3D. This demonstrates again that the energy flux ε by itself is not an appropriate measure of irreversibility and suggests the use of the dimensionless rate of change of the kinetic energy instead. A systematic statistical characterization of $W(\tau)$ can be formulated from its probability distribution function (PDF). Fig. 2*C* shows the PDF of $W(\tau)$ for several values of τ in the range $\tau_K\le\tau\le T$, where τ_K and T are the characteristic times at the dissipation scale l_D and the forcing scale l_F, respectively. The PDF of $W(\tau)$, normalized by its variance, exhibits wide tails, the more so as the value of τ is smaller. This feature is possibly related to intermittency, a characteristic phenomenon in turbulent fluids.

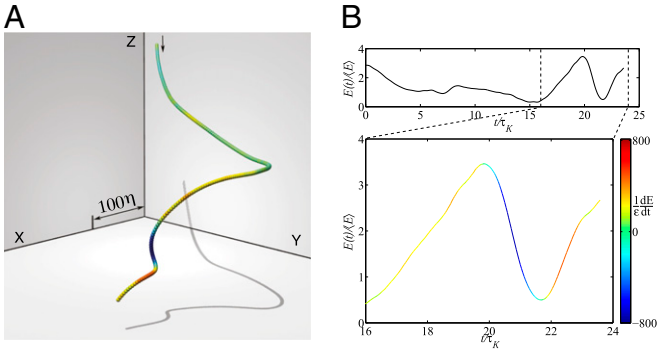

Fig. 1. Asymmetry of the statistics of energy differences. (*A*) The trajectory of a fluid particle in a 3D laboratory flow at $R_\lambda=690$. The color coding refers to the instantaneous power $p(t)=\mathrm{d}E/\mathrm{d}t=\mathbf{a}(t)\cdot\mathbf{V}(t)$ acting on the fluid particle, showing that energy builds up slowly and dissipates quickly. The particle enters the observation volume from above and leaves from below. The scale bar is expressed in terms of the Kolmogorov scale η, which is the dissipation scale of this flow, $l_D=\eta=30$ μm. (*B*) The evolution of the kinetic energy $E(t)$ of the same particle as a function of time, in units of the Kolmogorov time τ_K, the fastest time scale of the flow, characterizing the dynamics at scale l_D. *B*, *Upper* is for the entire trajectory, while *Lower* magnifies the period with strong energy change, i.e., high power fluctuations (same color coding as in *A*). The particle experiences higher values of negative p, compared with positive p, indicating that the particle loses kinetic energy more rapidly than gaining energy.

Could we understand the skewness of $W(\tau)$ in the framework of fluctuation theorems that have been established theoretically (22, 23), and verified experimentally (4)? For small systems in contact with thermostats, fluctuation theorems state that the probabilities of energy gaining and energy loss are related (2) by

$$\ln\left[\frac{P(-W)}{P(W)}\right]\propto W, \qquad [1]$$

which, at a first glance, is also suggested by the shape of the tails of PDFs in Fig. 2*C*. Our measurements of $\ln[P(-W)/P(W)]$ at different values of time-lag τ, shown in Fig. 2*D*, however, shows a more complicated dependence on W than the simple linear law **1**. This suggests that fluctuation theorems do not apply directly to tracer particles in turbulence. This we attribute to the properties of the forces acting on fluid particles, which are very different from the forces in usual thermodynamic systems (8).

Statistics of Power Fluctuations: Quantifying Detailed Balance Violations. As we demonstrate that the results obtained in the general context of stochastic thermodynamics do not apply to a small fluid element carried by the fluid, the asymmetry observed for the distribution of the energy differences along a trajectory (Fig. 2*C*) points to a more fundamental aspect, namely the breakdown of time reversibility in the system. In fact, as we show in the following, the third moment of $W(\tau)$ allows us to quantify the irreversibility, and to relate it to the range of scales in the system.

Let us consider the rate of change of the kinetic energy following a tracer particle, i.e., the power $p=\lim_{\tau\to0}[W(\tau)/\tau]=\mathrm{d}E/\mathrm{d}t=\mathbf{V}\cdot\mathbf{a}$, with $\mathbf{a}=\mathrm{d}\mathbf{V}/\mathrm{d}t$ being the fluid acceleration. At thermal equilibrium, time reversibility is equivalent to detailed balance in the sense that the probability of energy gain ($p>0$) is the same as the probability of energy loss ($p<0$) for any particle with any velocity. Asymmetric (skewed) PDFs of p, as shown in Fig. 3 *A* and *B*, are therefore a signature that detailed balance is violated. [We note that the statistics of the power p may be affected by specific, nonuniversal aspects of the forcing, especially in 2D, in which the external forcing acts at small scales and is fast-changing (*SI Text*).] This violation can then be quantified by odd moments of the fluctuations of p, which change sign when reversing $t\to-t$, thus enabling to detect whether the movie of turbulence is playing backwards or forwards (9). Similar to $W(\tau)$, the first moment of p vanishes for stationary and homogeneous flows. The third moment, which can be measured reliably, is sufficient to quantify the violation of detailed balance.

As already explained, a proper measure must be dimensionless. A natural choice is the dimensionless power p/ε, whose third moment, Ir, defined as

$$Ir=-\langle p^3\rangle/\varepsilon^3, \qquad [2]$$

allows us to measure irreversibility. Fig. 3 *C* and *D* show that Ir increases with the Reynolds number in both 2D and 3D, hence

PHYSICS

with the separation of scales between forcing and dissipation. In 3D, it grows approximately as $Ir \propto R_\lambda^2$, where $R_\lambda \propto (l_F/l_D)^{2/3}$ is the Taylor-scale Reynolds number for 3D turbulence. For 2D turbulence in the energy cascade regime, i.e., $l_F \ll l_D$, we characterize the scale separation by the friction-based Reynolds number $R_\alpha \propto (l_D/l_F)^{2/3}$ (*SI Text*). The data from both experiments and numerics shown in Fig. 3*D* demonstrate that irreversibility grows also with this Reynolds number approximately as $Ir \propto R_\alpha^2$. The second moment, $\langle p^2\rangle/\varepsilon^2$, grows with the Reynolds numbers as $R_\alpha^{4/3}$ and $R_\lambda^{4/3}$, as shown in Fig. 3 *E* and *F*. As a consequence, the skewness of the power fluctuations, defined as $s = \langle p^3\rangle/\langle p^2\rangle^{3/2}$, is approximately constant over the range of Reynolds numbers investigated in both 2D and 3D.

Thus, remarkably, the measure of irreversibility, *Ir*, directly accessible in laboratory flows, depends on the Reynolds number to a simple power, independent of the specificity of the forcing, and even more surprisingly, of the directions of the energy flux.

We note that the dependence of the moments $\langle (p/\varepsilon)^n\rangle$ as $R_\lambda^{2n/3}$ or $R_\alpha^{2n/3}$ for $n = 2$ and 3 does not extend to higher values of n, consistent with the observation that the PDFs of p/ε are not self-similar, and depend on the Reynolds number (*SI Text*).

Scaling of Power and Flight–Crash Events

The results documented in Figs. 2 and 3 establish a clear relation between the moments of the power, hence of the energy differences, and the Reynolds number. The aim of this section is to provide simple phenomenological arguments to interpret the dependence found in Fig. 3, which is observed both in 2D and 3D and seems universal.

First, let us note that the Lagrangian velocity difference does not have self-similar statistics, so it is reasonable to assume that there are events with different scaling exponents γ for the velocity change, $\delta V(\tau) \propto \tau^\gamma$. Different γ contribute different velocity moments. Landau–Obukhov phenomenology (14) suggests $\delta V(\tau) \simeq (\varepsilon\tau)^{1/2}$, which physically corresponds to velocity diffusion under the action of random short-correlated forces. If particle acceleration (energy increase) would proceed in this way, one would expect $\langle p^2\rangle \propto \langle a^2\rangle \propto R_\lambda$. Our results of $\langle p^2\rangle \propto R_\lambda^{4/3}$ on power moments, as shown in Fig. 3, thus make it reasonable to assume that another type of events exists, where a fast particle takes flight and then sharply decelerates (by pressure gradient and/or viscous friction) to acquire the velocity of its neighbors. During such a flight, the particle travels a distance $\sim V\tau$ and the velocity difference across such distance can be estimated by the Kolmogorov estimate $\delta V(\tau) \simeq (\varepsilon V\tau)^{1/3}$. This estimate rests on the assumption that the Eulerian field remains essentially frozen during the time τ. Note that this velocity change is much larger than the one suggested by Landau–Obukhov, $(\varepsilon V\tau)^{1/3}/(\varepsilon\tau)^{1/2} = (T/\tau)^{1/6}$, thus such events must be rare. Therefore, it is unlikely that these rare flight–crash events dominate the Lagrangian structure functions $\langle[\delta V(\tau)]^n\rangle$, especially for small values of n. As we now demonstrate, however, the scaling of the power suggests that such events provide the main contribution to the moments of the energy changes and power, which are determined by the correlation between **V** and δ**V**. The flight and crash picture suggests for times in the inertial interval

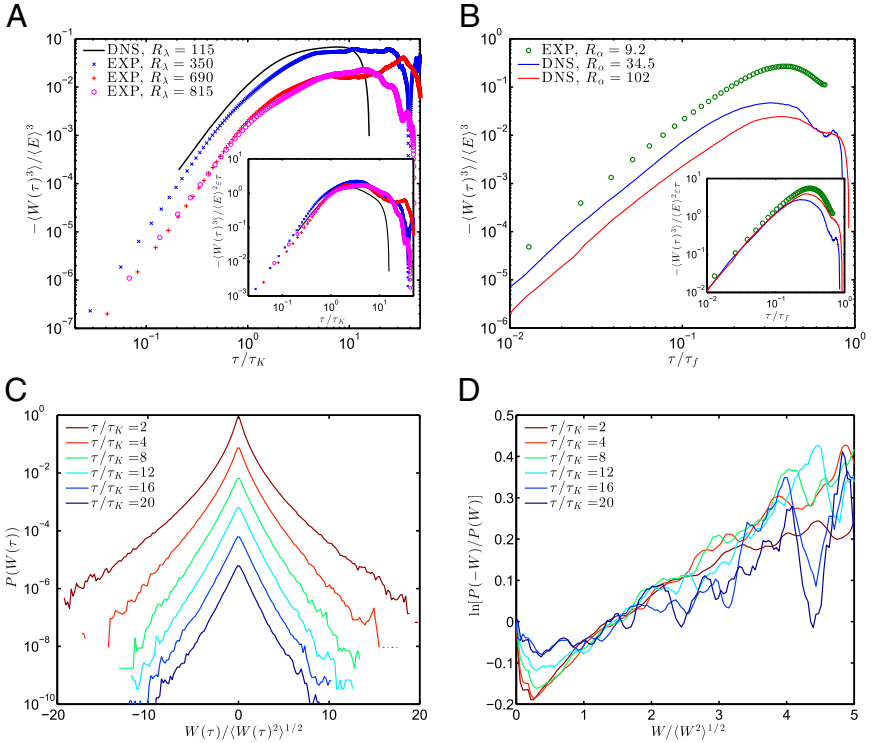

Fig. 2. (*A*) The third moment of energy increments $W(\tau) = E(t+\tau) - E(t)$ as a function of τ in 3D turbulence for different Reynolds numbers from both experiments (EXP) and direct numerical simulations (DNS). The quantity $-\langle W(\tau)^3\rangle$ grows like τ^3 at short times. The curves obtained at different Reynolds numbers collapse once scaled using **[3]** (*Inset*). (*B*) The third moment of $W(\tau)$ from 2D turbulence experiments. Features similar to 3D turbulence are observed, i.e., $\langle W^3(\tau)\rangle$ is negative and nearly saturates when $\tau/\tau_f \sim 1$, where $\tau_f \sim (l_F^2/\varepsilon)^{1/3}$ is the characteristic time corresponding to scale l_F (*SI Text*). (*C*) PDFs of $W(\tau)$ at different values of τ, in the $\tau_K \le \tau \le T$ range, corresponding to 3D experimental flow at $R_\lambda = 350$. The values of $W(\tau)$ are normalized by their rms values. For clarity, the PDFs have been shifted by a factor of 10 from each other. The PDF tails can be plausibly represented by exponentials. (*D*) The logarithm of the ratios of the probability of $-W$ and W as a function of W ($W > 0$) at different values of τ. The linear prediction of **[1]**, which has been shown to apply in many systems in presence of several thermostats, does not simply apply for turbulence.

$$W(\tau) \approx V \cdot \delta V \sim V^{4/3}(\varepsilon\tau)^{1/3}. \quad [3]$$

This scaling for the energy change means that the Lagrangian quantity proportional to ε is the third-order structure function of the energy difference, $\langle W^3(\tau)\rangle \propto U_{rms}^3(\varepsilon U_{rms}\tau)$. This suggests that the smooth scaling $\langle W^3(\tau)\rangle \propto \tau^3$ at $\tau \ll \tau_K$ turns into $\langle W^3(\tau)\rangle \propto \varepsilon\tau$ at $\tau \gg \tau_K$. Accordingly, we normalize the third moment of W by $U_{rms}^4\varepsilon\tau$, as shown in Fig. 2*A*, *Inset*. The very good collapse of the data in 3D gives support for the flight-crash picture discussed here. Using the same scaling in 2D leads to a very good collapse of the curves for very small τ. The difference between Fig. 2 *A* and *B* at longer times may be a manifestation of the very different physics occurring in 2D and 3D flows. The finite-time average power $W(\tau)/\tau$ behaves as $V\delta V/\tau \sim V(V\varepsilon\tau)^{1/3}/\tau \sim \varepsilon(T/\tau)^{2/3}$. It increases when τ decreases and saturates at $\tau \simeq \tau_K$, since $W(\tau) \propto \tau$ for $\tau \lesssim \tau_K$. The moments of the instantaneous power can therefore be deduced from **[3]** using the saturation value $p \approx W(\tau_K)/\tau_K \sim \varepsilon(T/\tau_K)^{2/3}$, which leads to $\langle p^3\rangle \propto \varepsilon^3(T/\tau_K)^2 \propto \varepsilon^3 R_\lambda^2$ and $\langle p^2\rangle \propto \varepsilon^2 R_\lambda^{4/3}$ as observed in Fig. 3. The scaling provided by **[3]** also explains the systematic dependence of $\langle W^3(\tau)\rangle/\langle E\rangle^3$ as a function of the Reynolds number (*SI Text*).

Discussion

Turbulence is characterized by large fluctuations. Notoriously, the local energy dissipation rate shows strong spatial fluctuations, which are known to play a key role in the origin of intermittency, or fluctuations of other quantities of the turbulent flow (10). Much work has been devoted to the modeling of fluctuations of the local dissipation rate and of its coarse-grained generalization, especially in relation to devising approximate numerical schemes (13). Here we are interested in the related but different question of the exchange between a very small subsystem, a fluid particle, and the surrounding turbulent flow, in the spirit of work done for small systems in contact with thermostats (3). The comparison of our results with those described by stochastic thermodynamics, therefore, reveals the general features of systems very far from thermal equilibrium.

The main achievement of this work has been to document and quantify the intrinsic irreversibility of turbulent flows. This led us

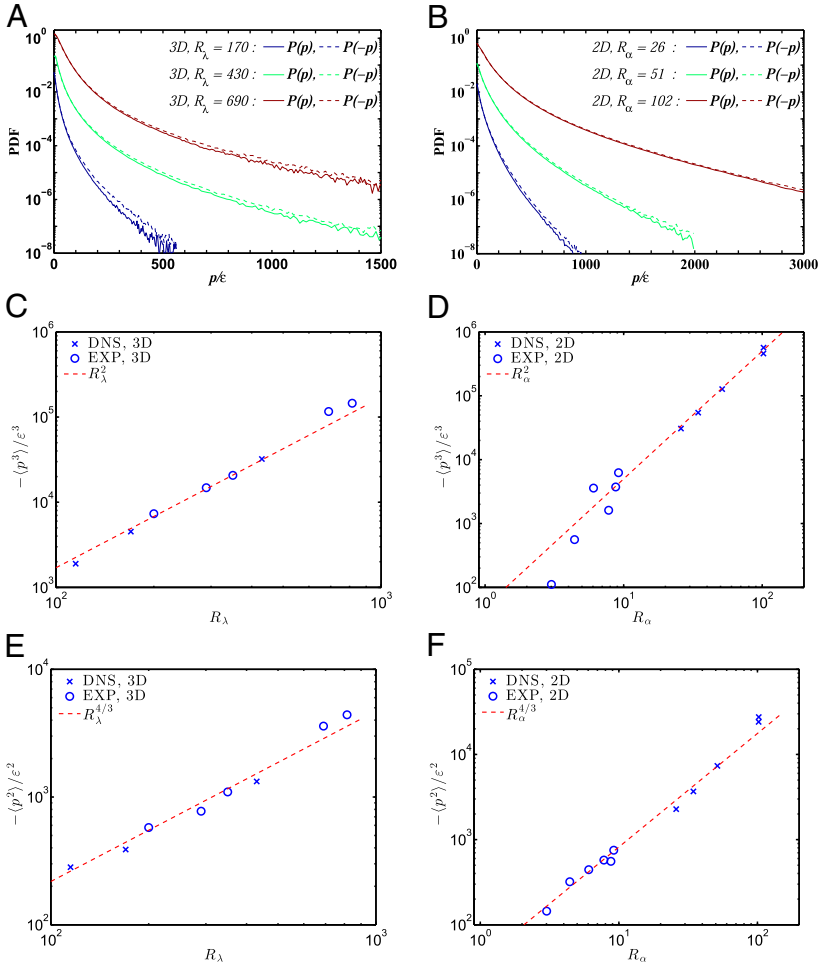

Fig. 3. (*A*) The PDFs of p/ε at three different Reynolds numbers $R_\lambda = 170$, 430, and 690 for 3D turbulence. For comparison, the PDFs of negative power ($p < 0$), shown by the dashed lines, are reflected around the vertical axis. The characteristic power is much larger than ε and increases with the Reynolds number. Moreover, large negative values of p are more frequent than large positive values, indicating that most of the violent energy exchange events that a fluid particle experiences are energy-loss events rather than energy gaining. Data at $R_\lambda = 170$ and 430 are from DNSs and data at $R_\lambda = 690$ are from experiments. (*B*) PDFs of p/ε from 2D turbulence simulations at $R_\alpha = 26$, 51, and 102. Similar behavior as for 3D turbulence is observed. (*C–F*) Statistical properties of the instantaneous power p acting on fluid particles. (*C*) Variation of $-\langle p^3\rangle/\varepsilon^3$ vs. R_λ for 3D turbulence. Its increase is close to R_λ^2. (*D*) Variation of $-\langle p^3\rangle/\varepsilon^3$ vs. R_α for 2D turbulence, which increases approximately as R_α^2. (*E* and *F*) Variation of $\langle p^3\rangle/\varepsilon^3$ for 3D and 2D turbulence, respectively. The variance increases rapidly with Reynolds numbers, close to $R_\lambda^{4/3}$ or $R_\alpha^{4/3}$ for 3D and 2D turbulence. This results in a skewness nearly independent of the Reynolds number: $\langle p^3\rangle/\langle p^2\rangle^{3/2} \approx -0.5$ in 3D and ≈ -0.20 in 2D.

to define a quantity *Ir*, which increases as a power law when the Reynolds number increases, i.e., when the flow becomes more turbulent. Remarkably, this way of characterizing turbulent flows is insensitive to the direction of energy flux through spatial scales.

The observation of asymmetry in the time dependence of the kinetic energy of particle in a turbulent flows should be contrasted with the spatial asymmetry, observed in particular in the case of a passive scalar with an imposed gradient (24). In this case, the asymmetric, ramp-and-cliff structure results from a large scale forcing (the gradient), and persists all the way to very small scales. A weaker analogy has been documented in shear flows (25, 26). The phenomenon documented here is very different, as the temporal asymmetry is found both for direct and inverse cascades. It would be interesting to understand whether the possible connection between $\langle W^3(\tau)\rangle$ and the third-order Eulerian structure function point to any particular flow structures (27). We merely notice here that the sizes shown in Fig. 1*A* make any apparent relation with vortex tubes, observed many times before (15), unlikely.

Our results stress the main difference between the well-studied case of systems in contact with thermostats, and those involving a cascade through scales such as turbulence. In this context, our approach could shed new light on a variety of different problems, such as plasma turbulence (28), quantum turbulence (29), magnetohydrodynamics (30), and more generally, on any system that is irreversible and has a separation of scales. The investigation of such systems in the spirit of the present work is likely to lead to new concepts in the physics of the nonequilibrium.

Materials and Methods

We describe briefly the different turbulent flows that we analyzed in both 3D and 2D and in both physical experiments and numerical simulations. More details can be found in *SI Text*.

Experimental Setups. The turbulent flows that we generated in laboratory experiments include the 3D von Kármán flows, 2D turbulence driven either electromagnetically or by surface ripples (Faraday waves).

von Kármán flows in 3D. The 3D experiments were performed in a so-called von Kármán mixer, which generates high-Reynolds-number turbulent water flow between two counterrotating disks (15, 17). We measured 3D trajectories of tracer particles seeded in the flow using optical Lagrangian particle tracking (17, 18). The Reynolds number of the turbulence was in the $350 \le R_\lambda \le 690$ range. The effects induced by the weak inhomogeneity of the flow at the center of the apparatus, where the measurements were carried out, can be shown to be small (*SI Text*).

Two-dimensional turbulence experiments. Energy is injected into flows by driving horizontal vortices whose scale is much smaller than the size of the container. In electromagnetically driven turbulence such vortices are driven by the Lorenz force produced by the spatially varying vertical magnetic field and the electric current flowing across the fluid cell in electrolyte. In the Farady-wave-driven turbulence the vorticity is generated at the scale approximately at half of the wave period (31). The injected energy is then spread by the inverse energy cascade over a broad range of scales to form the Kolmogorov–Kraichnan spectrum. The 2D particle trajectories are tracked for a long time, up to 100 Lagrangian integral times (32).

Direct Numerical Simulations. The numerical work is based on simulating the Navier–Stokes equations,

$$\partial_t \mathbf{u} + \mathbf{u}\cdot\nabla\mathbf{u} = -\nabla P + \nu\nabla^2\mathbf{u} + \mathbf{f} - \alpha\mathbf{u}, \qquad [4]$$

where $\mathbf{u}(\mathbf{x},t)$ is the fluid velocity at location $\mathbf{x}$ and at time t. The velocity field is incompressible $\nabla\cdot\mathbf{u}=0$, a constraint which is imposed with the help of the pressure field P. The flow is forced by using an external field $\mathbf{f}$, which varies at a characteristic scale l_F. The viscous term $\nu\nabla^2\mathbf{u}$ acts to dissipate energy. For 2D flows, a linear friction is introduced through the $-\alpha\mathbf{u}$ term ($\alpha=0$ in 3D), to prevent the accumulation of energy at scales larger than $l_D=\alpha^{-3/2}\varepsilon^{1/2}$.

The Lagrangian information is then obtained by integrating in time the equation of motion of fluid tracers

$$\frac{d\mathbf{X}}{dt} = \mathbf{V}(t) = \mathbf{u}(\mathbf{X},t), \qquad [5]$$

in which the tracer velocity $\mathbf{V}(t)$ is the same as the fluid velocity $\mathbf{u}$ at position $\mathbf{X}$ and time t.

In all cases a statistically stationary flow was maintained by balancing the forcing and the dissipation terms. All the simulations discussed here were carried out in a periodic domain using standard pseudospectral methods.

In 3D, the simulations reported here used up to 384^3 modes. The flow was forced at a scale l_F comparable to the size of the domain, while energy was dissipated at the Kolmogorov scale η, $\eta = l_D = (\nu^3/\varepsilon)^{1/4}$, which was the smallest scale resolved in the simulation. The turbulence Reynolds numbers were $R_\lambda = 115$ and 170. Additionally, we used the flow field at $R_\lambda = 430$ made available from the Johns Hopkins University database (33).

The simulations of 2D flows reported here were carried out with up to $8{,}192^2$ modes. Forcing acted at a small scale l_F only, and energy was damped by friction that acts at a scale l_D, comparable to the size of the system.

ACKNOWLEDGMENTS. We thank the Kavli Institutes for Theoretical Physics (KITP), where the work started during the 2011 The Nature of Turbulence program (KITP) and continued during the 2012 New Directions in Turbulence program (KITP China). We also acknowledge partial support from the Max Planck Society, the Humboldt Foundation, and European Cooperation in Science and Technology Action MP0806 Particles in Turbulence. The work was supported by grants from the German Science Foundation (XU/91-3), the Minerva Foundation, the Bi-National Science Foundation, Agency of Natural Resources Grant Turbulent Evaporation and Condensation 2, the Australian Research Council Discovery Projects funding scheme (DP110101525), and a Discovery Early Career Research Award (DE120100364).

1. Onsager L (1931) Reciprocal relations in irreversible processes. *Phys Rev* 37:405–426.
2. Derrida B (2007) Non-equilibrium steady states: Fluctuations and large deviations of the density and of the current. *J Stat Mech* 9:P07023.
3. Seifert U (2012) Stochastic thermodynamics, fluctuation theorems and molecular machines. *Rep Prog Phys* 75(12):126001.
4. Ciliberto S, Joubaud S, Petrosyan A (2010) Fluctuations in out-of-equilibrium systems: from theory to experiment. *J Stat Mech* 12:P12003.
5. Chertrite R, Falkovich G, Gawedzki K (2008) Fluctuation relations in simple examples of non-equilibrium steady states. *J Stat Mech* 8:P08005.
6. Pomeau Y (1982) Symétrie des fluctuations dans le renversement du temps. *J Phys* 43(6):859–867.
7. Pine DJ, Gollub JP, Brady JF, Leshansky AM (2005) Chaos and threshold for irreversibility in sheared suspensions. *Nature* 438(7070):997–1000.
8. Rose HA, Sulem PL (1978) Fully developed turbulence and statistical mechanics. *J Phys* 39(5):441–484.
9. Falkovich G, Sreenivasan K (2006) Lessons from hydrodynamic turbulence. *Phys Today* 59(4):43–49.
10. Frisch U (1995) *Turbulence: The Legacy of A. N. Kolmogorov* (Cambridge Univ Press, Cambridge, UK).
11. Kraichnan RH (1967) Inertial ranges in two-dimensional turbulence. *Phys Fluids* 10(7):1417–1423.
12. Boffetta G, Ecke RE (2012) Two-dimensional turbulence. *Annu Rev Fluid Mech* 44:417–451.
13. Pope SB (2000) *Turbulent Flows* (Cambridge Univ Press, Cambridge, UK).
14. Falkovich G, et al. (2012) On Lagrangian single-particle statistics. *Phys Fluids* 24(5): 055102.
15. La Porta A, Voth GA, Crawford AM, Alexander J, Bodenschatz E (2001) Fluid particle accelerations in fully developed turbulence. *Nature* 409(6823):1017–1019.
16. Yeung PK (2002) Lagrangian investigations of turbulence. *Annu Rev Fluid Mech* 34:115–142.
17. Bourgoin M, Ouellette NT, Xu H, Berg J, Bodenschatz E (2006) The role of pair dispersion in turbulent flow. *Science* 311(5762):835–838.
18. Xu H, Pumir A, Bodenschatz E (2011) The pirouette effect in turbulent flows. *Nat Phys* 7(9):709–712.
19. Helbing D (2001) Traffic and related self-driven many-particle systems. *Rev Mod Phys* 73(4):1067–1141.
20. Jensen MH, Johansen A, Simonsen I (2003) Inverse statistics in economics: The gain-loss asymmetry. *Physica A* 324(1):338–343.
21. Mordant N (2001) PhD thesis. Mesure Lagrangienne en Turbulence : mise en oeuvre et analyse (Ecole Normale Supérieure de Lyon, Lyon, France).
22. Evans DJ, Cohen EGD, Morriss GP (1993) Probability of second law violations in shearing steady states. *Phys Rev Lett* 71(15):2401–2404.
23. Gallavotti G, Cohen EGD (1995) Dynamical ensembles in nonequilibrium statistical mechanics. *Phys Rev Lett* 74(14):2694–2697.
24. Shraiman BI, Siggia ED (2000) Scalar turbulence. *Nature* 405(6787):639–646.
25. Pumir A, Shraiman BI (1995) Persistent small scale anisotropy in homogeneous shear flows. *Phys Rev Lett* 75(17):3114–3117.
26. Shen X, Warhaft Z (2000) The anisotropy of the small scale structure in high Reynolds number ($R_\lambda \sim 1000$) turbulent shear flow. *Phys Fluids* 12(11):2976–2989.
27. Vainshtein SI, Sreenivasan KR (1994) Kolmogorov's 4/5th law and intermittency in turbulence. *Phys Rev Lett* 73(23):3085–3088.

28. Krommes JA (2002) Fundamental statistical description of plasma turbulence in magnetic fields. *Phys Rep* 360(1):1–352.
29. Paoletti MS, Lathrop DP (2011) Quantum turbulence. *Annu Rev Condens Matter Phys* 2:213–234.
30. Verma MK (2004) Statistical theory of magnetohydrodynamic turbulence: recent results. *Phys Rep* 401(5):229–381.
31. Francois N, Xia H, Punzmann H, Shats M (2013) Inverse energy cascade and emergence of large coherent vortices in turbulence driven by Faraday waves. *Phys Rev Lett* 110(19):194501.
32. Xia H, Francois N, Punzmann H, Shats M (2013) Lagrangian scale of particle dispersion in turbulence. *Nat Commun* 4:2013.
33. Li Y, et al. (2008) A public turbulence database cluster and applications to study Lagrangian evolution of velocity increments in turbulence. *J Turbul* 9(31):1–29.

Supporting Information

Xu et al. 10.1073/pnas.1321682111

SI Text

1. Energy Flux in Turbulence

We first briefly review some elementary concepts of energy flux in fluid turbulence. As explained in the introductory section of the main text, energy is injected into a turbulent flow at a scale l_F that is very different from the scale at which it is dissipated, l_D. The scale ratio l_F/l_D is large in 3D, $l_F/l_D \gg 1$, while it is small in 2D, $l_F/l_D \ll 1$. This property can be derived directly from the Navier–Stokes equations,

$$\frac{\partial \mathbf{u}}{\partial t} + \mathbf{u}\cdot\nabla\mathbf{u} = -\nabla P + \nu\nabla^2\mathbf{u}, \qquad [S1]$$

where $\mathbf{u}(\mathbf{x},t)$ is the velocity field, $P(\mathbf{x},t)$ is the pressure field (divided by the constant density), and ν is the kinematic viscosity.

In this work, we consider statistically stationary and homogeneous turbulent flows. In this case, an identity, known as Kolmogorov's 4/5 law (1), holds for scales intermediate between l_D and l_F (the inertial range of scales of turbulence)

$$\left\langle (\delta_r u)^3 \right\rangle = \gamma_D \varepsilon r, \qquad [S2]$$

where $\delta_r u$ is the longitudinal component of the velocity difference, $\delta_r u = [\mathbf{u}(\mathbf{x}+\mathbf{r}) - \mathbf{u}(\mathbf{x})]\cdot\mathbf{r}/r$ ($r = |\mathbf{r}|$), ε is the dissipation rate of energy, and the coefficient of proportionality γ_D depends on the spatial dimension D, $\gamma_3 = -4/5$ in 3D and $\gamma_2 = 3/2$ in 2D.

Whether energy flows towards larger or smaller scales depends on the sign of γ_D in this exact scaling relation, which is at the root of the deep difference in the nature of the energy flux in 2D and 3D turbulence. To see this, one derives from the Navier–Stokes equations an exact relation for the energy contained in a shell of wave numbers by decomposing the energy into Fourier series, and then integrating the components of the Fourier modes whose wave vectors are smaller than a maximum value K (1). The results can be interpreted as an energy budget per scale, in which the term originating from the nonlinear term in the Navier–Stokes equations, $(\mathbf{u}\cdot\nabla)\mathbf{u}$, is responsible for the flux of energy in the wave-number space. The sign of the flux is given by the sign of the coefficient γ_D in Eq. **S2**. Specifically, in 3D, $\gamma_3 < 0$ and the energy flux is towards large wave vectors or equivalently towards small scales. This leads to a direct cascade of energy. On the contrary, in 2D, $\gamma_2 > 0$, the energy flux is towards small wave vectors, or large scales, which leads to an inverse cascade. This fundamental distinction makes 2D and 3D turbulence properties very different. This is the reason why we have systematically investigated flows in both spatial dimensions.

In the inertial range, the characteristic time τ_r at a scale r, can be obtained from energy transfer considerations as $\tau_r = (r^2/\varepsilon)^{1/3}$ (up to a numerical constant) (1). In 3D, the time scale at the large (forcing) scale, l_F, is simply denoted as $T = (l_F^2/\varepsilon)^{1/3}$. The smallest length scale of the flow, the Kolmogorov length is given by $l_D = (\nu^3/\varepsilon)^{1/4}$, and the associated small time scale is known as the Kolmogorov time scale, $\tau_K = (l_D^2/\varepsilon)^{1/3} = (\nu/\varepsilon)^{1/2}$. In 2D, the characteristic time at the forcing scale is $\tau_f = (l_F^2/\varepsilon)^{1/3}$, whereas the time scale at the large scale, above which friction prevails, is $T = (l_D^2/\varepsilon)^{1/3}$. We note that the ratio between the characteristic time scales at the largest and smallest scales of the flow effectively correspond to the definition of the Reynolds number of the flow: $R_\lambda \propto T/\tau_K$ in 3D and $R_\alpha \propto T/\tau_f$ in 2D (see section 8 below for more detail).

In the following sections we discuss the experimental (section 2) and numerical (section 3) methods in 3D. The numerical simulation of 2D turbulence is described in section 4. We have performed two different types of experiments in 2D, both of which produce inverse cascade regimes, but are forced using very different protocols (section 5). Finally, section 6 provides more information on the asymmetry of the energy increments, whereas section 7 discusses the effects of forcing in relation with the results discussed briefly in *Results*. Finally, we discuss in section 8 the similarities between the Reynolds numbers that we defined for describing 2D and 3D turbulence.

2. Three-Dimensional Turbulence Experiments

In this section we describe the turbulent flow generating apparatus, the measurement technique, and the data processing used to obtain the velocities and accelerations following Lagrangian trajectories in 3D turbulence. Data from the same experiments have been used in other studies and have been reported, e.g., as in the supplementary information of ref. 2. We include here the detailed description for completeness.

2.1. The von Kármán Swirling Flow. The experiments were carried out in a von Kármán swirling water flow between two counter-rotating baffled disks. The apparatus has been described in detail in ref. 3. The flow is confined in a cylindrical plexiglas tank with an inner diameter of 48.3 cm and a volume of 120 L. The propellers are 20 cm in diameter, each with 12 vertical vanes 4.3 cm in height. The axial distance between the propellers is 33 cm. On each end of the tank, eight vanes are installed on the tank wall to suppress large-scale rotation (see figures 11 and 12 in ref. 3). The propellers are driven by two independently controlled direct current (DC) motors, each with 0.9-kW nominal power output. The rotation frequencies of the propellers are measured by photoelectrical sensors, which are then fed back to regulate the voltage applied on the DC motors to maintain the rotation of the propellers at desired frequencies. The long-time averaged frequencies of the two propellers are within 0.01% of the set value and the instantaneous fluctuations of each of the propellers are less than 1%. In the steady state, the mean flow in the apparatus may be decomposed into the shearing motion due to the rotation of the propellers and the pumping motion due to the centrifugal force (figure 11 in ref. 3). In the center of the tank, far from the propellers and the tank wall, the fluctuation velocity is much greater than the mean velocity. Our measurements were conducted in a cubic region of size approximately 2 cm in the center of the apparatus, where the local mean velocity is less than 20% of the local fluctuation velocity. In addition, the variation of the local level of fluctuations over this volume is less than 10%. Therefore, we consider turbulence in this region to be approximately homogeneous. Due to the axisymmetric forcing, the von Kármán flow is anisotropic at large scales. This anisotropy persists even at the highest Reynolds number that we have measured (3). However, since the quantities that we are considering here are traces of second-rank tensors, such as the instantaneous power $p \equiv \mathbf{u}\cdot\mathbf{a} = \sum_{i=1}^{3} u_i a_i$, the anisotropy of the flow affects our results only weakly. Note that in the center of the apparatus, where we performed our measurements, the particles lose kinetic energy on average, i.e., $\langle p\rangle \approx -\varepsilon$. This loss of energy is compensated by the flux of energy from the boundary (where the flow is set into motion) to the center region of the apparatus (4). Thus, the flow is not strictly homogeneous. The effect of this weak inhomogeneity on the third moments of the power fluctuations, defined by [2] of the main text, will be discussed in section 7.2.

2.2. Particle Tracking Measurement. The Lagrangian trajectories of the fluid were obtained by optically following tracer particles seeded in the flow. The tracer particles were polystyrene spheres with diameters of 26 μm and densities of 1.06 g/cm^3. Previous studies have shown that in our apparatus, these particles follow the water flow faithfully at Reynolds number up to $R_\lambda \sim 10^3$ (see, e.g., ref. 3). These tracer particles were illuminated by pulsed frequency-doubled neodymium-doped yttrium aluminum garnet lasers, with intensity up to 130 W. Their motion was then recorded by three high-speed complementary metal oxide semiconductor (CMOS) cameras from different viewing angles. Finally, the images were processed to obtain particle trajectories in 3D space and in time (5). Fluctuations of the laser light intensity and noise in the measurement system resulted in occasional interruptions of the particle trajectories. Using information in the position–velocity space allowed us to connect the segments belonging to the same trajectory (6). In this paper, we report on the statistics from measurements with Taylor microscale Reynolds number in the $350 \le R_\lambda \le 815$ range (see also ref. 7). In order to resolve the fastest changes of the turbulence, we chose our frame rates to have at least 15 measurements per Kolmogorov time τ_K. Using a Gaussian fitting method to locate particle center, we could achieve a spatial resolution of approximately 0.1 pixels (5), from which we could differentiate to obtain fluid acceleration with high accuracy. Table S1 in the supplementary information of ref. 2 summarized the parameters of the measurement system used in the experiments.

2.3. Data Processing. To obtain fluid particle velocities and accelerations, we first filtered the measured positions using a Gaussian filter and then differentiated the smoothed trajectories. The smoothing and differentiation were combined into one convolution using a kernel that is the derivative of the Gaussian filter (8). It should be pointed out that, because many tracer particles were tracked simultaneously, our measurements gave us also access to Eulerian information, such as the Eulerian structure functions. In particular, we computed the second-order velocity structure functions, from which we determined the turbulent energy dissipation rate ε. For example, measurements of $D_{LL}(r) \equiv \langle [(\mathbf{u}(\mathbf{x}+\mathbf{r},t) - \mathbf{u}(\mathbf{x},t)) \cdot \mathbf{r}/r]^2 \rangle$ and the inertial range scaling $D_{LL}(r) = C_2(\varepsilon r)^{2/3}$ led to $\varepsilon = [D_{LL}(r)/C_2]^{3/2}/r$. Furthermore, we used another exact inertial range relation, $\langle [\mathbf{u}(\mathbf{x}+\mathbf{r},t) - \mathbf{u}(\mathbf{x},t)] \cdot [\mathbf{a}(\mathbf{x}+\mathbf{r},t) - \mathbf{a}(\mathbf{x},t)] \rangle = -2\varepsilon$, to determine ε (see ref. 2 and references therein). These different methods of determination of ε gave values within $\pm 10\%$. We used the averaged value of the energy dissipation rate to compute other derived parameters such as the Taylor microscale Reynolds number R_λ.

3. Three-Dimensional Numerical Simulations

The results of direct numerical simulation (DNS) of 3D turbulent flows presented in this work came either from simulations at a relatively low Reynolds number, obtained directly using a pseudospectral code, or from the database developed at Johns Hopkins University (9).

3.1. The DNS at $R_\lambda = 115$ and $R_\lambda = 170$. The simulation code solved the 3D Navier–Stokes equations, Eq. **S1**, in a periodic cubic box of size 2π, using pseudospectral methods with up to 384^3 modes. The flow was maintained statistically stationary by keeping a fixed energy in the low wave-number modes, $|k| \le 1.5$, which evolve according to truncated Euler equations. The resulting flow had zero mean velocity, and the velocity fluctuations were shown to be statistically homogeneous and isotropic (10).

We took care that the smallest scale of the flow, the Kolmogorov length scale, η, defined by $\eta = (\nu^3/\varepsilon)^{1/4}$, was adequately resolved. In practice, the product $k_{max} \cdot \eta$ was larger than ~ 1.4. The results discussed in *Results* correspond to flow Reynolds numbers, based on the Taylor scale λ, $R_\lambda = \lambda u'/\nu = 115$ and 170, with 192^3 and 384^3 modes, respectively.

The trajectories of tracer particles were determined by integrating directly the equation of motion of tracer particles,

$$\frac{d\mathbf{X}}{dt} = \mathbf{V}(t) = \mathbf{u}(\mathbf{X},t). \qquad \textbf{[S3]}$$

We used the algorithm originally described in ref. 11. The acceleration was obtained by differentiating the velocity following the fluid particle.

The data for $R_\lambda = 115$ were obtained by following 130,000 particles for approximately 18 eddy turnover times, with a sampling time of $\sim 1/70$ of the eddy turnover time. In comparison, the statistics for the run at $R_\lambda = 170$ were determined by following 10^6 particles over one eddy turnover time. The sampling time corresponds to $1/100$ of the eddy turnover time.

3.2. The DNS at $R_\lambda = 430$ from the Johns Hopkins Turbulence Database. To obtain information on flows at larger Reynolds numbers, we used the turbulence database developed at Johns Hopkins University (9). The data has been obtained by simulating the Navier–Stokes equations with $1{,}024^3$ modes. The corresponding flow Reynolds number is $R_\lambda = 430$, with a resolution such that $k_{max} \cdot \eta = 1.38$. The velocity field and its derivatives are available over one full eddy turnover time (9).

From the database we obtained 16 snapshots of the velocity field, each consisting of $128 \times 256 \times 512$ spatial points. The 16 snapshots were equally separated over the one full eddy turnover time. The total number of statistics obtained is then 2.7×10^8 for instantaneous quantities.

In order to determine the correlation between velocity and acceleration discussed in *Results*, we used the following expression for the acceleration of tracer particles (note that the pressure is already divided by density):

$$\frac{d\mathbf{V}}{dt} = \mathbf{a} = -\nabla P + \mathbf{f} + \nu\nabla^2\mathbf{u}. \qquad \textbf{[S4]}$$

We determined the pressure gradient, forcing, and viscous terms using the functions provided from the database (9). From Eq. **S4**, the instantaneous power is expressed as

$$p \equiv \mathbf{V} \cdot \frac{d\mathbf{V}}{dt} = \mathbf{u} \cdot \mathbf{a} = -\mathbf{u} \cdot \nabla P + \mathbf{u} \cdot \mathbf{f} + \nu\mathbf{u} \cdot \nabla^2\mathbf{u}. \qquad \textbf{[S5]}$$

Note that in DNS, under the condition of perfectly steady states, the average instantaneous power following particles should be zero. In all simulations, the small fluctuations of the total kinetic energy inside the computational domain induced a small unbalance between the energy injected and the energy dissipated. As a result, the average instantaneous power was nonzero even after averaging over a few large-eddy turnover times. However, this residual average power is small compared to the turbulence energy dissipation rate, i.e., $\langle p \rangle / \varepsilon \approx 0$, much smaller than what is found in the experiments.

4. Two-Dimensional Numerical Simulations

We performed numerical simulations of the Navier–Stokes equation for a 2D incompressible velocity field, $\mathbf{u} = (u, v)$,

$$\frac{\partial\mathbf{u}}{\partial t} + \mathbf{u} \cdot \nabla\mathbf{u} = -\nabla P + \nu\nabla^2\mathbf{u} - \alpha\mathbf{u} + \mathbf{f}, \qquad \textbf{[S6]}$$

in which a linear friction term, $-\alpha\mathbf{u}$, was added to the Navier–Stokes equation to remove energy and to prevent energy pile up at large scales. In the absence of dissipation and of forcing, Eq. **S6** conserves both the mean kinetic energy $\langle E \rangle = (1/2)\langle u^2 + v^2 \rangle$ and

the mean enstrophy $\langle Z\rangle = (1/2)\langle\omega^2\rangle$, where $\omega = \nabla\times\mathbf{u}$ is the vorticity (12). The forcing term $\mathbf{f}$ injects energy and enstrophy in the system at rates ε_I and η_I, respectively, and their ratio is related to the characteristic scale of forcing $l_F = (\varepsilon_I/\eta_I)^{1/2}$.

According to the Kraichnan theory of 2D turbulence (12, 13), the energy injected in the system at scale l_F goes to larger scales at a rate ε_α, developing the inverse cascade (with a Kolmogorov–Kraichnan spectrum), while enstrophy flows to smaller scales at a rate η_ν, generating the direct cascade. The inverse cascade stops at the scale l_α, determined by friction: $l_\alpha \simeq \alpha^{-3/2}\varepsilon_\alpha^{1/2}$. The viscous scale, at which the direct enstrophy cascade is stopped, is $l_\nu \simeq \nu^{1/2}\eta_\nu^{-1/6}$. In the inertial range of scales, between l_α and l_F, the inverse energy cascade develops, whereas between l_F and l_ν, we have the direct cascade of enstrophy. For the purpose of this work, l_α acts as the dissipation scale: $l_D = l_\alpha$.

In the asymptotic limit of vanishing α and ν (i.e. $l_\nu \to 0$ and $l_\alpha \to \infty$) all the energy flows to large scales, $\varepsilon_\alpha = \varepsilon_I$, and the enstrophy to small scales, $\eta_\nu = \eta_I$. For finite values of the dissipative parameters, a residual fraction of energy, ε_ν, is dissipated by the viscous term in Eq. **S6** and similarly, a fraction of enstrophy, η_α, is dissipated by the friction term. Stationarity requires $\varepsilon_I = \varepsilon_\alpha + \varepsilon_\nu$ and $\eta_I = \eta_\alpha + \eta_\nu$. Simple balance of energy and enstrophy fluxes gives $\varepsilon_\nu/\varepsilon_\alpha \propto \nu$ (12), which is indeed observed in numerical simulations (14). A similar relation can be obtained for enstrophy fluxes.

For comparison with the 3D results, it is useful to introduce an equivalent of Taylor microscale Reynolds number for the inverse cascade, based on the extension of the inverse-cascade part of the inertial range as

$$R_\alpha \equiv (l_\alpha/l_F)^{2/3} = (\varepsilon_\alpha/\varepsilon_I)^{1/2}\eta_I^{1/3}\Big/\alpha. \qquad \textbf{[S7]}$$

With this definition, R_α does not depend on the viscosity. This short discussion suggests that finite Reynolds effects in 2D turbulence can be more subtle than in 3D as one should take the two limits $\nu \to 0$ and $\alpha \to 0$ simultaneously in order to recover the asymptotic theoretical predictions.

We have numerically integrated Eq. **S6** by means of a standard, fully de-aliased, pseudospectral code on a double periodic square domain of N^2 grid points, for a set of parameters given in Table S1. The forcing term was Gaussian with a correlation function $\langle \mathbf{f}(\mathbf{x},t)\cdot\mathbf{f}(\mathbf{x}',t')\rangle = F(r/l_F)\delta(t-t')$ with $r = |\mathbf{x}-\mathbf{x}'|$ and we choose $F(x) = F_0\exp(-x^2/2)$. The δ-correlation in time ensured the exact control of the energy injection rate. After the system reached stationary states, we computed separately all the terms on the right-hand side of Eq. **S6**, which gave the different contributions to the instantaneous power

$$p(\mathbf{x},t) = \mathbf{V}\cdot\frac{\mathrm{d}\mathbf{V}}{\mathrm{d}t} = \mathbf{u}\cdot\mathbf{a} = \mathbf{u}\cdot\left(-\nabla P + \nu\nabla^2\mathbf{u} - \alpha\mathbf{u} + \mathbf{f}\right) \qquad \textbf{[S8]}$$

and we collected the statistics for several large-scale eddy turnover times.

In Fig. S1 we plot the energy spectra for the different runs in stationary conditions. The extension of the inverse cascade range with the Kolmogorov spectrum $E(k)\sim k^{-5/3}$ increases with the decreasing of friction coefficient α, in agreement with Eq. **S7**.

5. Two-Dimensional Turbulence Experiments

2D turbulence was studied experimentally using two methods of turbulence generation: electromagnetically driven turbulence in layers of electrolyte and Faraday-wave-driven turbulence in vertically vibrated containers.

Electromagnetically driven turbulence (15) was produced in layers of electrolytes [here we used a Na_2SO_4 water solution, with specific gravity(SG) of 1.03] by running electric current $\mathbf{j}$ across the fluid cell. A matrix of magnetic dipoles placed underneath the cell produced spatially varying magnetic field $\mathbf{B}$, shown as red (upward ↑) and blue (downward ↓) regions in Fig. S2. In these experiments 900 magnets were used (30×30 matrix, 10 mm between adjacent magnets). The Lorenz $\mathbf{j}\times\mathbf{B}$ force produced 900 vortices, which determines the forcing wave number, $k_f \approx 630\ \mathrm{m}^{-1}$. To reduce the bottom drag and to avoid the influence of the bottom boundary layer, the electrolyte layer was placed on top of a heavier ($SG = 1.8$), nonconducting fluid (FC-3283, produced by 3M), which is immiscible with water.

Tracer particles (50 μm, polyamid, $SG = 1.03$) were suspended in the top layer and were illuminated using a 2-mm thick laser sheet parallel to the free surface. Particle motion was filmed using an Andor Neo scientific CMOS (sCMOS) camera.

We changed the spectral energy flux injected into the flow by varying the electric current. At low currents, spectral energy was localized in a relatively narrow wave number range around the forcing wave number. As the current was increased, forcing scale vortices merged, forming larger and larger eddies until the kinetic energy spectrum broadened and formed Kolmogorov–Kraichnan spectrum $E(k) = C\varepsilon^{2/3}k^{-5/3}$.

The experimental setup for the Faraday-wave-driven turbulence is shown in figure 1 of ref. 16. The horizontal motion of particles on the surface of vertically vibrated liquids shows statistical properties consistent with fluid motion in 2D turbulence (16). Here we performed experiments in a circular container (178 mm in diameter, 30 mm deep). The container was filled with a liquid to a depth larger than the wavelength of the perturbations at the surface. The monochromatic forcing was varied in the range of frequencies f_0 = 30–100 Hz. The dominant frequencies of the excited surface ripples were a factor of 2 lower, at the frequency of the first subharmonic of the excitation frequency, $f = f_0/2$. A diffusing light imaging technique was used to visualize the surface ripples along with floating particles added on it. A light-emitting diode panel was placed between the transparent bottom of the container and the shaker's top plate to illuminate the flow. High-resolution movies (800×800 pixels) were recorded in the range of 80–120 frames per second, using an Andor Neo sCMOS camera. Typically 2,000 particles were tracked simultaneously for over 300 frames using a particle-tracking algorithm.

The spectra of the horizontal velocity fluctuations measured at $f_0 = 60$ Hz at three vertical acceleration levels ($a/g = 0.7$, $a/g = 1.2$, and $a/g = 1.6$) have been shown in figure 3b of ref. 16, where a is the amplitude of the vertical acceleration and $g = 9.81\ \mathrm{m/s^2}$ is the gravity of the earth. These accelerations correspond to supercriticalities $\epsilon = (a - a_{th})/a_{th}$ in the $0.16 \le \epsilon \le 1.6$ range, where $a_{th} = 0.6\times g$ is the threshold of the parametric wave excitation. These spectra are close to the Kolmogorov–Kraichnan theory power law of $E(k) = C\varepsilon^{2/3}k^{-5/3}$ at $k \le 1,500\ \mathrm{m}^{-1}$. At higher wave numbers, $k > 1,550\ \mathrm{m}^{-1}$, spectra are typically steeper than the k^{-3}-expected direct enstrophy cascade, probably due to the strong viscous dissipation. At lower forcing frequencies, a clear k^{-3} is observed at $k > k_f$.

The Reynolds number in 2D experiments was defined as in the 2D numerical simulations: $R_\alpha = (l_D/l_F)^{2/3} = \varepsilon^{1/2}\alpha^{-3/2}/l_F^{2/3}$. In the experiments, the forcing scale l_F was fixed. The increase in R_α was achieved by enhancing ε, hence l_D. This is in contrast to numerical simulations where the increase in l_D, hence in scale separation R_α, resulted from the decrease in the linear dissipation α. It should be noted that in laboratory experiments the extent of the inertial interval at large scales was restricted by the size of the circular fluid container, which limited the range of R_α achievable.

For Faraday-wave-driven turbulence, the range of turbulence kinetic energy achievable at a given driving frequency f_0 can be dramatically varied by adjusting the vertical acceleration a. As shown in figure 3c of ref. 16, at $f_0 = 60$ Hz, the energy was increased by over 2 orders of magnitude as a varied from slightly higher than the threshold of parametric excitation ($0.6\times g$ in this case) to just below the threshold of droplet formation ($2.4\times g$).

6. Time Asymmetry of Energy Increments

6.1. Galilean Invariance. In this work, we are interested in the change of kinetic energy $E(t)=(1/2)\mathbf{V}(t)\cdot\mathbf{V}(t)$ following a single fluid particle in turbulence. In particular, we study the energy increment over a time lag τ: $W(\tau)=E(t+\tau)-E(t)$ and the instantaneous rate of kinetic energy change, $p(t)=\mathrm{d}E/\mathrm{d}t=\mathrm{d}W/\mathrm{d}\tau=\mathbf{a}\cdot\mathbf{V}$. For a given turbulent flow field $\mathbf{u}(\mathbf{x},t)$, the kinetic energy associated with the absolute motion of a fluid particle is not a Galilean invariant variable. Because of the lack of Galilean invariance, we explicitly choose to work here with the kinetic energy of velocity fluctuations, $\mathbf{V}$, defined as $\mathbf{V}=\mathbf{u}-\langle\mathbf{u}\rangle$, where $\langle\mathbf{u}\rangle$ is the mean velocity, which is a constant in homogeneous flows. The fluctuation velocity $\mathbf{V}$ can be viewed as seen by an observer who follows N fluid particles at the same time. Then the best choice for the observer is to move at the averaged velocity $(1/N)\sum_i^N\mathbf{u}^{(i)}$, which approaches the mean velocity when the number N increases. Our analyses are within the frame of reference that moves with the mean velocity. In this sense, even the fluctuation velocity following a single particle, $\mathbf{V}(t)$, contains information on more than one particle. Note that for all the flows we investigated, the mean flow vanishes, $\langle\mathbf{u}\rangle\cong 0$. Our discussion here is merely to suggest how to extend our work to the cases with nonvanishing mean flows. We emphasize that in any case, our analysis involves only single-particle statistics. We are not considering multiparticle statistics in this work.

6.2. Probability Distribution Function of Energy Increments. As we stated earlier, we restrict ourselves to statistically stationary and homogeneous flows. For such flows, the first moments of both $W(\tau)$ and p vanish: $\langle W(\tau)\rangle=0$ and $\langle p\rangle=0$. Time asymmetry is therefore reflected in the probability distribution functions (PDFs) of W and p around 0.

Fig. 2 *A–C* showed that the PDFs of the differences in the kinetic energy along trajectories, $W(\tau)$, are skewed, i.e., not symmetric around $W=0$. We document here in detail how this asymmetry varies as a function of the time-lag τ. Fig. S3 shows the PDFs of $W(\tau)$ for several values of τ, ranging from the dissipative scale ($\tau=0.3\tau_K$, bottom curve in Fig. S3) to the integral scale ($\tau=9.6\tau_K\approx T$, top curve in Fig. S3). The data corresponds to a Reynolds number, $R_\lambda=115$. For the sake of clarity, the curves have been shifted by a factor of 10 with respect to one another. The dashed lines correspond to negative values of W, reflected with respect to the y axis, while the continuous lines show the PDF for positive values of W. Fig. S3 shows that the difference between the dashed curves and the continuous line remains roughly constant, consistent with the observation in Fig. 2*A*. While the asymmetry remains constant, a systematic change of shape is observed when the ratio τ/τ_K increases. Namely, the tails of the PDF become straight, suggesting an exponential distribution of W at large values of $|W|$ (see in particular the upper curves of Fig. S3).

The exponential tails of the distribution of W can be qualitatively justified when $\tau/\tau_K\gtrsim 1$, by using the fact that (*i*) individual velocity distributions are almost Gaussian and (*ii*) the two velocities at time t and $t+\tau$ become almost independent. However, the observation that the difference between the distributions for $W<0$ and $W>0$, as measured by the third moment of the distribution, remains roughly constant up to values of τ comparable to T, which demonstrates that even over a long time fluid particles are sensitive to the asymmetry induced by time irreversibility.

6.3. Asymmetry Between Energy Gains and Losses. Fig. S4 shows the comparison of the PDFs of instantaneous power $p=\mathbf{V}\cdot\mathbf{a}$, weighed with $|p|^3$, for configuration where the energy of the particle increases ($p>0$) and for configurations where the energy of the particles diminishes ($p<0$). It is clear that for large values of $|p|$, the configurations where $p<0$ have a higher probability. The plot also shows that at least for $\langle p^3\rangle$, our results are statistically converged.

Results shown in Fig. S4 clearly demonstrate that the distribution is not self-similar, i.e., the PDF of $(p/\varepsilon)R_\lambda^{-2/3}$ depends on Reynolds number. Yet, remarkably, the third moment of p/ε does scale as the second moment in the power 3/2, i.e., as R_λ^2 (Fig. 3). This phenomenon is reminiscent of the intermittency effect on velocity increments: While lower-order moments seem to follow rather well the predictions of the K41 theory, the deviations become more and more significant for higher-order moments. However, the accuracy of our data does not allow us to draw any firm conclusion on higher-order statistics of the power p.

6.4. Reynolds Number Dependence of the Third Moment of *W*. Fig. 2*A* shows the third moment $\langle W^3(\tau)\rangle$, normalized by the third power of $\langle E\rangle$, the average kinetic energy of particles in the flow, as a function of τ/τ_K. The dependence on the Reynolds number of the curves shown in Fig. 2*A* can be readily deduced from the good collapse of $\langle W^3\rangle/[\langle E\rangle^2(\varepsilon\tau)]$, shown in the *Inset*. This collapse implies that

$$\langle W^3(\tau_K)\rangle\sim\langle E\rangle^2\varepsilon\tau_K\sim\langle E\rangle^3(\tau_K/T)\sim\frac{\langle E\rangle^3}{R_\lambda}, \qquad \textbf{[S9]}$$

where we used the standard estimate for the energy dissipation rate, $\varepsilon\sim\langle E\rangle/T$. The relation **S9** therefore predicts that the curves shown in the main part of Fig. 2*A* are deduced from one another by a ratio proportional to R_λ. This relation explains very well the dependence observed in Fig. 2*A*.

We note that in 2D, the dependence of $\langle W^3(\tau)\rangle$ on the Reynolds number R_α does not seem to be as simple as in 3D. The scaling deduced from the flight-crash argument allows us to collapse the data only at small times, for $\tau\ll\tau_f$. This property is in fact a direct consequence of the scaling $\langle p^3\rangle/\epsilon^3\propto R_\alpha^2$. The dependence of $\langle W^3(\tau)\rangle/(\langle E\rangle^2\varepsilon\tau)$ on R_α, visible at times $\tau\sim\tau_f$, may point to systematic deviations with respect to our flight-crash argument. The difference between 2D and 3D can be interpreted as a manifestation of the deep differences between turbulent flows in different spatial dimensions, which remains to be explored further from the point of view of the analysis in this article.

7. Effects of Forcing on the Instantaneous Power

7.1. Influence of Forcing on the Power Statistics. Turbulence generally depends on the nature of forcing. Of most fundamental interest are the properties that are universal, i.e., independent of forcing.

In 3D, a large-scale force impacts strongly on the single-time statistics in the inertial interval via intermittency and anomalous scaling (17). On the other hand, the moments of the forcing term, $\mathbf{f}\cdot\mathbf{V}$, behave as $\langle(\mathbf{f}\cdot\mathbf{V})^n\rangle\sim\varepsilon^n$ as a function of the order n of the moment. The reason for this is that both $\mathbf{V}$ and $\mathbf{f}$ are quantities that vary on a large scale. In particular, the fluctuations of $\mathbf{f}$ are small compared to the fluctuations of the dissipation term (viscous or viscous plus friction) and ∇P. As a consequence, the contribution of $\langle(\mathbf{f}\cdot\mathbf{V})^3\rangle$ to the third moment of power $\langle(\mathbf{V}\cdot\mathbf{a})^3\rangle$ is small: The statistics of power are unaffected by the details of the forcing.

In 2D, the properties of the forcing may affect significantly the statistics of $\mathbf{V}\cdot\mathbf{a}$. The reason is that due to the inverse cascade, the forcing $\mathbf{f}$ varies on small scales, contrary to the velocity field $\mathbf{V}$ that is varying on large scales. The scalar product $\mathbf{f}\cdot\mathbf{V}$ then rapidly varies along a particle trajectory. Thus, the averaged quantity $\langle\mathbf{f}\cdot\mathbf{V}\rangle$ involves many cancellations. In particular, one could conceivably have $\varepsilon=\langle(\mathbf{f}\cdot\mathbf{V})\rangle\ll\langle(\mathbf{f}\cdot\mathbf{V})^2\rangle^{1/2}$, and similarly, $\langle(\mathbf{f}\cdot\mathbf{V})^3\rangle\gg\varepsilon^3$, implying that the details of the forcing may be important while studying the third moment of $\mathbf{V}\cdot\mathbf{a}$.

In the results from 2D numerical simulations in which white noise forcing is implemented, the sign of the third moment of $\mathbf{V}\cdot\mathbf{a}$ is negative. On the other hand, in turbulent flows induced by surface waves, the forcing is well correlated in time due to the coherency of the monochromatic Faraday waves at the frequency of $f_F = f_0/2$. This leads to a positive sign of $\langle(\mathbf{V}\cdot\mathbf{a})^3\rangle$. Due to this nature of turbulence forcing in these experiments, fluid particles are accelerated quickly by the waves at the time scale of $T_F = f_F^{-1}$, and then slowly lose energy via turbulence interactions. This property is a manifestation of the nonuniversal nature of forcing in 2D. However, since the time scales over which turbulent dynamics develop are much larger than T_F, averaging $\mathbf{V}\cdot\mathbf{a}$ in time along the trajectories over several periods of Faraday waves, i.e., defining $p(t) = (1/sm)\int_0^{sm}\mathbf{V}(t+t')\cdot\mathbf{a}(t+t')dt'$, where sm is the time period of averaging, eliminates the contribution of forcing on the $\mathbf{V}\cdot\mathbf{a}$ statistics, and reveals negative $\langle p^3\rangle$ in the inertial interval. Similarly, we filter the energy increments along the trajectories as $W(\tau) = (1/sm)\int_0^{sm}(1/2)[\mathbf{V}^2(t+\tau+t') - \mathbf{V}^2(t+t')]dt'$.

The contribution of forcing can be seen in the Lagrangian spectra of $\mathbf{V}^2$ and $\mathbf{V}\cdot\mathbf{a}$ computed along the tracer trajectories in the surface wave driven 2D turbulence. As shown in Fig. S5 *A* and *B*, the spectra exhibit strong peaks at a frequency close to f_F, corresponding to the Doppler-shifted Faraday wave frequency. Another peak seen at lower frequencies ($f \le 6$ Hz) corresponds to the turbulent motion, including the inertial range. Low-pass filtering $\mathbf{V}^2$, more precisely, averaging $\mathbf{V}^2$ over $sm = 2T_F$ along the trajectories as defined above, eliminates the forcing peak in the spectra of $\mathbf{V}^2$ (Fig. S5*A*). The data shown in Fig. 2*B* are obtained after applying this filtering with $sm = 2T_F$. On the other hand, the peaks at $\approx f_F$ are much more prominent in the spectra of $\mathbf{V}\cdot\mathbf{a}$ and contribute to a strong signal, which is responsible for the measured positive skewness of $\langle(\mathbf{V}\cdot\mathbf{a})^3\rangle$. Although smoothing $\mathbf{V}\cdot\mathbf{a}$ along the Lagrangian trajectories over $2T_F$ reduces significantly the relative contribution of the peak at $\approx f_F$ (Fig. S5*B*), the filtered signal still exhibits a positive skewness. In Fig. S5*C*, we show the skewness of the averaged power p as a function of sm, the time of averaging. As the filtering period is increased, the third moment $\langle p^3\rangle$ decreases and reaches an essentially constant negative value when the smoothing time is larger than $\sim 5T_F$ (Fig. S5*C*). A similar behavior is observed for all values of the vertical accelerations. The same values of the smoothing parameters are used for p and W by filtering $\mathbf{V}^2$ and $\mathbf{V}\cdot\mathbf{a}$ separately. To improve the statistical convergence in the determination of W, we systematically shifted the initial position along trajectories. In Fig. 3 *D* and *F* the second and the third moments of p from experimental data are computed by smoothing p over $7T_F$.

7.2. Implication for 3D Experimental Data. Note that in the 3D experiments, there is no stochastic body forcing, i.e., $\mathbf{f} = 0$. The turbulent flows are set into motion at the boundary. As explained at the end of section 2.1, this leads to a weak inhomogeneity in the volume of the experiment, and therefore to a small deviation from the idealistic stationary and homogeneous case considered in the main text.

In our measurement volume far away from the boundary, the averaged form of Eq. **S5** gives (4) $\langle p\rangle = \langle\mathbf{V}\cdot\mathbf{a}\rangle \approx \langle\nu\mathbf{u}\cdot\nabla^2\mathbf{u}\rangle = -\varepsilon$. This difference, compared with the situation analyzed in the main text and in the previous section, leads only to minor quantitative differences, as we now explain.

The existence of a nonzero mean of the instantaneous power, $\langle p\rangle \approx -\varepsilon$, results in small changes in the moments of p. However, as can be inferred from Fig. 3 *C* and *E*, the mean is only a very small fraction of the fluctuation for p: $\langle p\rangle/\langle p^2\rangle^{1/2} \approx -\varepsilon/\langle p^2\rangle^{1/2} \approx 10^{-2}$. Also, the ratio $\langle p^2\rangle\varepsilon/\langle p^3\rangle$ is smaller than $\sim 1/20$ in all the experiments presented here.

To check quantitatively the effect of the nonzero value of $\langle p\rangle$, we introduce the fluctuation, $p' = p - \langle p\rangle$. The moments of p' are

$$\frac{\langle p'^2\rangle}{\varepsilon^2} = \frac{\langle p^2\rangle}{\varepsilon^2} - \frac{\langle p^2\rangle}{\varepsilon^2} \approx \frac{\langle p^2\rangle}{\varepsilon^2} - 1 \approx \frac{\langle p^2\rangle}{\varepsilon^2}, \qquad \textbf{[S10]}$$

and similarly

$$\frac{\langle p'^3\rangle}{\varepsilon^3} \approx \frac{\langle p^3\rangle}{\varepsilon^3} + 3\frac{\langle p^2\rangle}{\varepsilon^2} - 2 \approx \frac{\langle p^3\rangle}{\varepsilon^3}. \qquad \textbf{[S11]}$$

The most sensitive quantity is probably the irreversibility *Ir*, which changes to

$$Ir' = \frac{\langle p'^3\rangle}{\langle p'^2\rangle^{3/2}} \approx Ir\left[1 - 3\frac{\langle p\rangle\langle p^2\rangle}{\langle p^3\rangle}\right] \approx Ir\left[1 + 3\frac{\langle p^2\rangle/\varepsilon^2}{\langle p^3\rangle/\varepsilon^3}\right]. \qquad \textbf{[S12]}$$

Using data from Fig. 3, we conclude that the relative change in *Ir* is smaller than about 10% for $R_\lambda \sim 10^3$, which is within the uncertainty of the measurements.

8. Definitions of Reynolds Numbers for 2D and 3D Turbulence

In this work, we used for 3D turbulent flows the Reynolds number based on the Taylor microscale R_λ. We defined a friction-based Reynolds number R_α for 2D flows. While the use of R_λ for 3D turbulence is standard, the introduction of R_α is less common, and may look arbitrary at first sight. Here we discuss briefly the similarities between these two Reynolds numbers, which are also the reason why we chose them.

Both R_λ and R_α are related to the scale separation l_F/l_D. More specifically, $R_\lambda \sim (l_F/\eta)^{2/3}$, where the Kolmogorov scale η is determined by the balance between viscous dissipation and the energy flux, $\eta = (\nu^3/\varepsilon)^{1/4}$, and $R_\alpha \sim (l_\alpha/l_F)^{2/3}$, where $l_\alpha \sim (\varepsilon/\alpha^3)^{1/2}$ is determined by the balance between frictional dissipation and the (inverse) energy flux. In both cases, the forcing scales l_F may be regarded as "bulk quantities," since they are set by the design of the apparatuses (propeller size, magnet spacing, etc.). On the other hand, the scales η and l_α, corresponding to dissipation, are set by quantities which are the result of turbulent fluctuations, controlled by the (fluctuating) energy flux. These scales are thus completely independent of the size of the apparatus. In 3D, the scale η explicitly depends on the viscosity, and could be modified by using a different fluid. Similarly, the scale l_α can be adjusted by changing the friction coefficient α, as in 2D numerical simulations, or by increasing the energy flux in 2D experiments (see the description of 2D experiments in section 4).

The nature of the fluctuations determining the dissipative length scales, l_D and η, however, depends strongly on the spatial dimension. The fluctuations in l_D in 2D should be smaller than those of η in 3D because they are coming from large scales and therefore, involve an averaging process.

The main feature that needs to be kept in mind is that both R_λ and R_α measure scale ratios, which reflect the number of degrees of freedom in a large system undergoing turbulent dynamics, irrespective of the spatial dimension. What we showed in this paper is that the two Reynolds numbers are related to the third moment of the power statistics, which means that the number of degrees of freedom and the measure of the time irreversibility in fact grow together. The fact that similar laws are observed in two systems whose dynamics are significantly different may point to more general principles, yet to be discovered.

A journal club lecture on this work by Ms. Anna Frishman from the Weizmann Institute is available from the Kavli Institute for Theoretical Physics at the University of California, Santa Barbara: http://online.kitp.ucsb.edu/online/waveflows14/frishman/.

1. Frisch U (1995) *Turbulence: The Legacy of A. N. Kolmogorov* (Cambridge Univ Press, Cambridge, UK).
2. Xu H, Pumir A, Bodenschatz E (2011) The pirouette effect in turbulent flows. *Nat Phys* 7(9):709–712.
3. Voth GA, La Porta A, Crawford AM, Alexander J, Bodenschatz E (2002) Measurement of particle accelerations in fully developed turbulence. *J Fluid Mech* 469:121–160.
4. Mann J, Ott S, Andersen JS (1999) *Experimental Study of Relative, Turbulent Diffusion* (Risø National Laboratory, Roskilde, Denmark), Technical Report Risø-R-1036(EN).
5. Ouellette NT, Xu H, Bodenschatz E (2006) A quantitative study of three-dimensional Lagrangian particle tracking algorithms. *Exp Fluids* 40(2):301–313.
6. Xu H (2008) Tracking Lagrangian trajectories in position-velocity space. *Meas Sci Technol* 19:075105.
7. Bourgoin M, Ouellette NT, Xu H, Berg J, Bodenschatz E (2006) The role of pair dispersion in turbulent flow. *Science* 311(5762):835–838.
8. Mordant N, Crawford AM, Bodenschatz E (2004) Experimental Lagrangian acceleration probability density function measurement. *Physica D* 193:245–251.
9. Li Y, et al. (2008) A public turbulence database cluster and applications to study Lagrangian evolution of velocity increments in turbulence. *J Turbul* 9(31):1–29.
10. Pumir A (1994) A numerical study of pressure fluctuations in three-dimensional, incompressible, homogeneous, isotropic turbulence. *Phys Fluids* 6(6):2071–2083.
11. Yeung PK, Pope SB (1988) An algorithm for tracking fluid particles in numerical simulations of homogeneous turbulence. *J Comput Phys* 79:373–416.
12. Boffetta G, Ecke RE (2012) Two-dimensional turbulence. *Annu Rev Fluid Mech* 44: 417–451.
13. Kraichnan RH (1967) Inertial ranges in two-dimensional turbulence. *Phys Fluids* 10(7): 1417–1423.
14. Boffetta G, Musacchio S (2010) Evidence for the double cascade scenario in two-dimensional turbulence. *Phys Rev E Stat Nonlin Soft Matter Phys* 82(1 Pt 2):016307.
15. Xia H, Shats M, Falkovich G (2009) Spectrally condensed turbulence in thin layers. *Phys Fluids* 21(12):125101.
16. Francois N, Xia H, Punzmann H, Shats M (2013) Inverse energy cascade and emergence of large coherent vortices in turbulence driven by Faraday waves. *Phys Rev Lett* 110(19):194501.
17. Falkovich G, Sreenivasan K (2006) Lessons from hydrodynamic turbulence. *Phys Today* 59(4):4349.

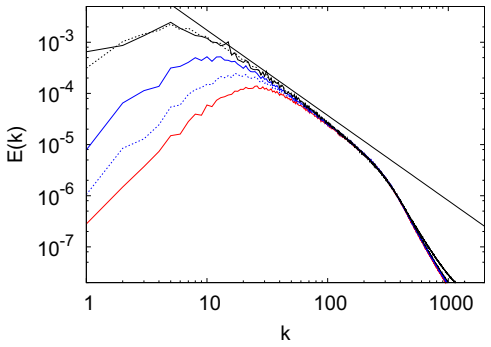

Fig. S1. Kinetic energy spectra from 2D simulations at stationary states. Curves with different line styles correspond to the different runs listed in Table S1. Run A, red solid; run B, blue dashed; run C, blue solid; run D, black dashed; run E, black solid. The black straight line represents Kolmogorov scaling $k^{-5/3}$.

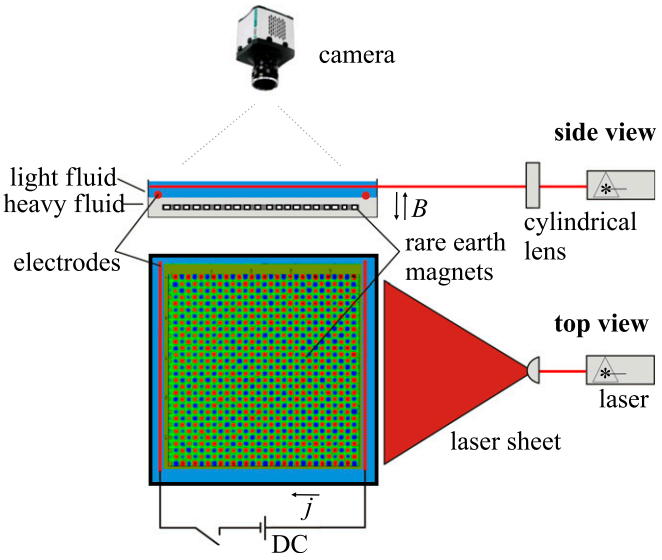

Fig. S2. Experimental setup for the electromagnetically driven turbulence.

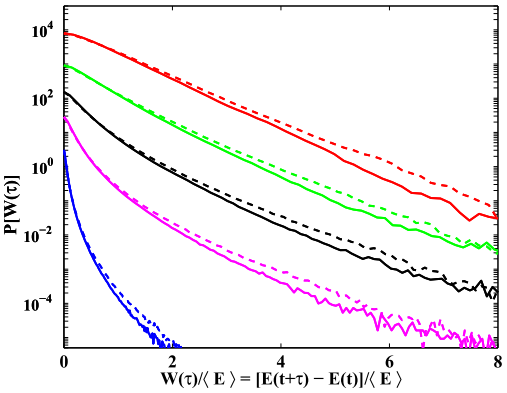

Fig. S3. PDFs of the velocity difference at several values of τ ($\tau/\tau_K = 0.3$, 1.2, 2.4, 4.8, and 9.6) from the 3D DNS at $R_\lambda = 115$. The PDFs have been shifted upwards for clarity by a factor of 10 with respect to the previous ones. The curves corresponding to negative values of W have been reflected with respect to the vertical axis, and are shown with dashed lines.

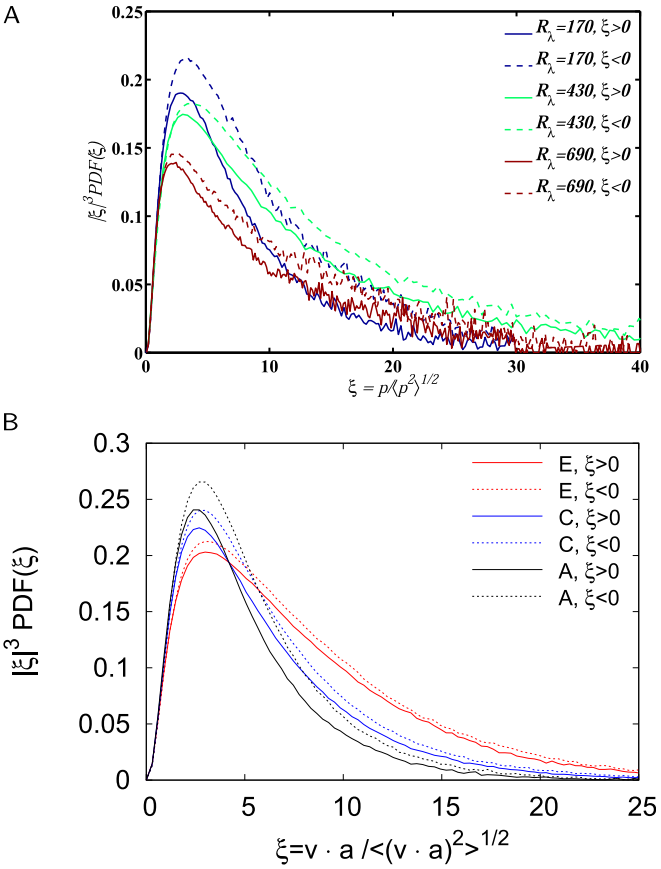

Fig. S4. PDFs of the instantaneous power $p = \mathbf{V} \cdot \mathbf{a}$ weighted with p^3 for energy-gaining events, $p > 0$ (solid lines), and for energy-losing events, $p < 0$ (dashed lines). (*A*) Data from 3D experiments and DNS and (*B*) from 2D simulation runs A, C, and E, with Reynolds numbers $R_\alpha = 25.9$, 51.4, and 102.3, respectively.

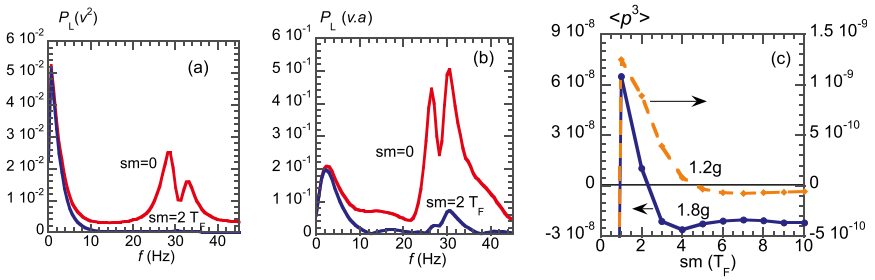

Fig. S5. Spectral signature of the forcing and the effect of filtering. Panels (*A*) and (*B*) show the Lagrangian spectra of the kinetic energy $\mathbf{V}^2$ and the instantaneous power $\mathbf{V}\cdot\mathbf{a}$, respectively. The curves in red are the raw spectra (without filtering), which exhibit a peak at $f \approx f_0/2$, corresponding to the forcing, in addition to the peaks at low frequency ($f \approx 2$ Hz) corresponding to the turbulent degrees of freedom. Low-pass filtering the signals, with a cutoff corresponding to twice the period of the forcing $sm = 2T_F$, considerably reduces the peak at $f_0/2$, as shown by the blue curves, although the peak is still visible in the spectrum of filtered $\mathbf{V}\cdot\mathbf{a}$. (*C*) Convergence of $\langle p^3 \rangle$, the third moment of the filtered power, as a function of the smoothing parameter *sm*. The dashed orange curve corresponds to a forcing acceleration of $a = 1.2$ g, and the full, blue curve to a forcing acceleration of $a = 1.8$ g.

Table S1. Parameters of the 2D simulations

Run	A	B	C	D	E
N	4,096	4,096	4,096	4,096	8,192
$\nu \times 10^6$	2.3	2.3	2.3	2.3	1.0
α	0.08	0.06	0.04	0.02	0.02
R_α	25.9	34.5	51.4	102.0	102.3
$\varepsilon_\alpha/\varepsilon_I$	0.72	0.71	0.70	0.69	0.83
η_ν/η_I	0.85	0.87	0.92	0.96	0.95

α, friction coefficient; ε_α, the rate of energy dissipation by friction; ε_I, energy injection rate; η_I, enstrophy injection rate; η_ν, the rate of enstrophy dissipation by viscosity; N, spatial resolution; R_α, friction-based Reynolds number; ν, viscosity.